ACS Catalysis

pubs.acs.org/acscatalysis
Research Article

First-Principles-Based Kinetic Monte Carlo Simulations of Methane Steam Reforming on Stepped Ni Surfaces

Zeyu Wu, Sai Sharath Yadavalli, Carlos Fonte, and Michail Stamatakis*

Cite This: https://doi.org/10.1021/acscatal.6c01172
Read Online

ABSTRACT: Methane Steam Reforming (MSR) is a critical process for hydrogen production in the chemical industry. Nickel-based catalysts are usually preferred for MSR due to their high activity and low cost. Several studies have shown that step edges and defects on Ni surfaces have a strong influence on the MSR kinetics. However, a detailed mechanistic-level understanding of the MSR reaction on stepped Ni surfaces has remained elusive. In this work, we have developed a DFT-parameterized Kinetic Monte Carlo (KMC) model to investigate the detailed kinetics of MSR reaction on stepped Ni surfaces (which contain step and terrace sites) and compare them systematically against the (111) facet. Comparisons of the predicted MSR turnover frequencies (TOFs) on Ni(211) and Ni(111) surfaces indicate that the TOF on Ni(211) exhibits strong temperature dependence, whereas Ni(111) is more sensitive to the partial pressure of CH_4. Additionally, we found that the step sites are more active in adsorbing and dissociating water, suggesting that higher water partial pressure improves Ni(211) performance. To further understand the role of step sites, we extended our analysis by changing the density of the step sites in the KMC lattice, providing insights into the broader impact of step density on catalytic behavior. These findings contribute to a deeper understanding of the reaction mechanisms governing MSR on stepped Ni surfaces, offering valuable insights for optimizing catalyst design and improving hydrogen production efficiency.

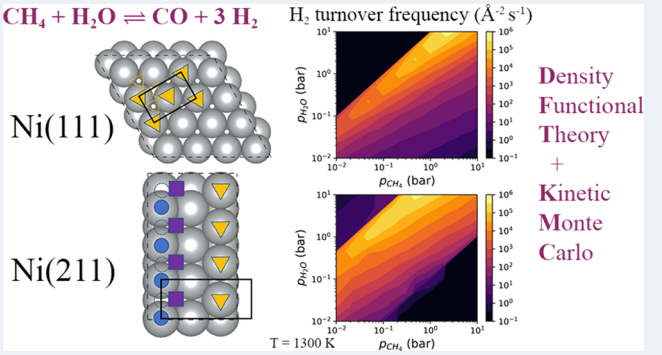

KEYWORDS: *catalysis, kinetic Monte Carlo, density functional theory, methane steam reforming, nickel, catalytic activity, structure sensitivity*

1. INTRODUCTION

In the global transition toward sustainable energy systems, hydrogen has gained increasing attention as a clean and efficient energy carrier, capable of decarbonizing multiple sectors.[1] Among all production methods, methane steam reforming (MSR) remains the most dominant and cost-effective route, currently responsible for over 95% of global hydrogen production.[2−4] At the industrial scale, the MSR reaction operates at 600–900 °C and 10–30 bar.[5] The relevant pathways can be classified into four categories: (i) Methane dissociation (which forms CH_x intermediates), (ii) Water dissociation (which leads to the formation of hydroxyl and oxygen species), (iii) oxidation pathways (where C and CH react with O and OH), and (iv) reactions giving rise to the final products (syngas: CO(g) and H_2(g)).[6−8] Nickel (Ni)-based catalysts are widely used in MSR due to their high activity for C–H scission and relative affordability.[9] However, Ni catalysts are highly susceptible to carbon poisoning (coking) under MSR operating conditions, which leads to blockage of active sites, and, in severe cases, mechanical damage through the growth of carbon whiskers.[10,11] Understanding and mitigating coke formation is thus central to improving catalyst life span and process efficiency. Most mechanistic studies of MSR on Ni have focused on the flat Ni(111) surface due to its thermodynamic stability.[12−14] However, growing evidence from experiments and density functional theory (DFT) calculations suggests that stepped surfaces such as Ni(211) are more reactive and play a critical role in initiating carbon nucleation and whisker growth.[15,16] The under-coordinated atoms at step edges are more prone to hydrocarbon decomposition, making the Ni(211) facet especially relevant for understanding coking behavior.

DFT investigations of key MSR elementary reactions on Ni(111) and Ni(211) indicate that, for most steps, the Ni(211) surface has lower activation barriers than Ni(111).

Received: February 10, 2026
Revised: March 31, 2026
Accepted: April 7, 2026

https://doi.org/10.1021/acscatal.6c01172
ACS Catal. XXXX, XXX, XXX−XXX

Nevertheless, DFT models are inherently limited by the assumptions of 0 K temperature and vacuum conditions, and thus, fail to capture the reaction kinetics under the operating conditions of MSR. More generally, recent work by Lozano-Reis et al.,[17] has shown that the dominant reaction mechanism inferred from static DFT energetics may differ substantially from the results obtained via kinetic modeling under realistic catalytic conditions once coverage effects, site availability, and pathway competition are explicitly taken into account. This highlights the limitation of assigning the dominant catalytic pathway from DFT energetics alone in complex reaction networks, and further motivates the use of kinetic modelling approaches. In order to study the influence of operating conditions, Blaylock et al. developed a DFT-parameterized mean-field microkinetic model (MKM) that provided an integrated description of three facets Ni(111), Ni(100) and Ni(211).[18] Their multifaceted scheme reproduced overall methane-conversion trends better than a terrace-only model, confirming the catalytic relevance of step sites.

However, the same study also underscored the intrinsic limitations of the mean-field approach: (i) aside from empirical corrections to the adsorption energies to indirectly account for C*–C*/CH*–CH* adsorbate-adsorbate lateral interactions, such interactions are otherwise neglected, even though coverages on Ni(211) and Ni(100) were substantial; (ii) by averaging over all surface sites it neglects the spatial fluctuations that are responsible for whisker-carbon nucleation and step blocking. This limitation is further exemplified in the recent work by Gracia et al.,[19] which systematically compared mean-field microkinetic model results with CE-based KMC simulation predictions for CO_2 hydrogenation on Ni(111). It was thus shown that while the two approaches are in closer agreement at low surface coverages, KMC is a more reliable method for predicting accurate kinetics under high-coverage conditions where adsorbate interactions and spatial correlations play a critical role. These shortcomings motivate the adoption of higher-fidelity techniques, such as the graph-theoretical kinetic Monte Carlo (KMC),[20−23] which captures explicitly spatial inhomogeneities, treats lateral interactions in detail using cluster expansion Hamiltonians and Brønsted-Evans-Polanyi relations, and captures complex chemistries between adsorbates in detail.

In this work, we develop a first-principles-based KMC model to elucidate the MSR kinetics on Ni(211) as well as other stepped surfaces, and draw a comparison against Ni(111), which contains only terrace sites. By simulating the performance of these surfaces across varying temperatures and partial pressures, we conduct sensitivity analyses to understand how the oxidation pathways are influenced by reaction conditions. We find that the TOF of MSR on Ni(211) exhibits a strong temperature dependence, whereas the TOF of MSR on Ni(111) is more sensitive to pressure variations. At industrial operating conditions, the MSR TOFs on Ni(111) surface were predicted to be much higher than Ni(211) due to the lower levels of surface coverage. Additionally, step sites demonstrate a greater ability to adsorb and dissociate water, suggesting that higher water partial pressure improves Ni(211) performance, while it reduces Ni(111) performance. Furthermore, KMC flux analysis was carried out to identify the dominant reforming pathways on the Ni(111) and Ni(211) surfaces. Moreover, by combining insights from both facets, this study provides a step toward modelling the realistic behavior of Ni nanoparticles, which inherently expose a mix of terrace and stepped sites. These results provide a deeper insight into the mechanism by which step sites alter the MSR kinetics.

2. METHODS

2.1. DFT Calculations

In this study, all DFT calculations were performed using the Vienna *Ab initio* Simulation Package (VASP) 5.4.4.[24−26] The exchange-correlation component of the Kohn-Sham theory was approximated by employing the Perdew-Burke-Ernzerhof (PBE) functional, and dispersion (van der Waals) interactions were included using the D3 method.[27] This choice was based on the results of the benchmarks by Yadavalli et al.,[28] who identified PBE-D3 as a suitable functional for capturing the MSR and coking chemistries on the Ni surface. The clean slab DFT model consists of a 6-layer $p(3 \times 4)$ supercell of Ni(211), with the bottom three layers frozen, the top view of the lattice is depicted in Figure 1a. Periodic slab images were separated by 16 Å of vacuum, and a dipole correction was applied to all slab calculations.[29] The electronic step tolerance was set to 10^{-7} eV. Furthermore, the conjugate gradient optimization technique was utilized, aiming to converge the forces acting on each atom to less than 0.01 eV/Å. The plane wave energy cutoff was set to 400 eV, and the projector augmented wave (PAW) method[30] was adopted to model the interactions between core and valence electrons. The Brillouin zone was sampled using a $6 \times 5 \times 1$ Monkhorst-Pack k-point grid.[31]

The transition state (TS) search calculations were conducted by using the ML-NEB module of CatLearn[32−34] and the Dimer method.[35] Furthermore, the identified TS geometries (saddle points in the potential energy surface) were refined by using the quasi-Newton method[36] and validated by performing vibrational analyses. The latter clearly show that all of the TS structures only have one imaginary mode, which represents the bond stretching for the corresponding elementary event of MSR (refer to Table S1). All crystal structure manipulations and data analysis were carried out using the Python Materials Genomics package (pymatgen)[37] and the Atomic Simulation Environment (ASE).[38] The MSR DFT dataset of Ni(111) was obtained from a previous study.[39]

The formation energies of the adsorbates were computed using as reference states the corresponding clean slab (e.g. Ni(111) or Ni(211) as appropriate), as well as CH_4(g), H_2O(g) and H_2(g) as the reference gas species. In eq 1, EF^A is the formation energy of adsorbate A, E_{DFT}^{A+slab} is the DFT energy of the adsorbate-Ni slab system, $E_{DFT}^{slab}$is the DFT energy of the Ni clean slab, $E_{DFT}^{CH_4(g)}$, $E_{DFT}^{H_2(g)}$, and $E_{DFT}^{H_2O(g)}$ represent the gas-phase DFT energies of methane, hydrogen, and water, respectively:

$$EF^A = E_{DFT}^{A+slab} - E_{DFT}^{slab} - \left(nE_{DFT}^{CH_4(g)} + mE_{DFT}^{H_2(g)} + rE_{DFT}^{H_2O(g)}\right) \quad (1)$$

The stoichiometry between the adsorbate's atoms and those of the gas-phase reference species is balanced out using the real numbers n, m and r. For instance, the formation energy calculation of the CHO adsorbate would have $n = 1$, $m = -2.5$, and $r = 1$.

2.2. KMC Calculations

All kinetic simulations were conducted using the *Zacros* software,[21] which implements the graph-theoretical KMC approach to model complex chemistries on the surfaces of heterogeneous catalysts. In *Zacros*, adsorbate-adsorbate lateral interactions are captured using cluster expansion (CE) Hamiltonians, and the influence thereof on the activation energies of elementary events are modeled via Brønsted-Evans-Polanyi relations.[22] The rate constants for each elementary step are computed by employing the transition state theory (TST). Under the TST formulation, the pre-exponential factors involve (quasi)partition functions of reactants and transition states.[21,40] Thus, the partition functions of gas-phase species were computed using the free translator, rigid rotor, and harmonic oscillator models, while, for adsorbed species,

https://doi.org/10.1021/acscatal.6c01172
ACS Catal. XXXX, XXX, XXX−XXX

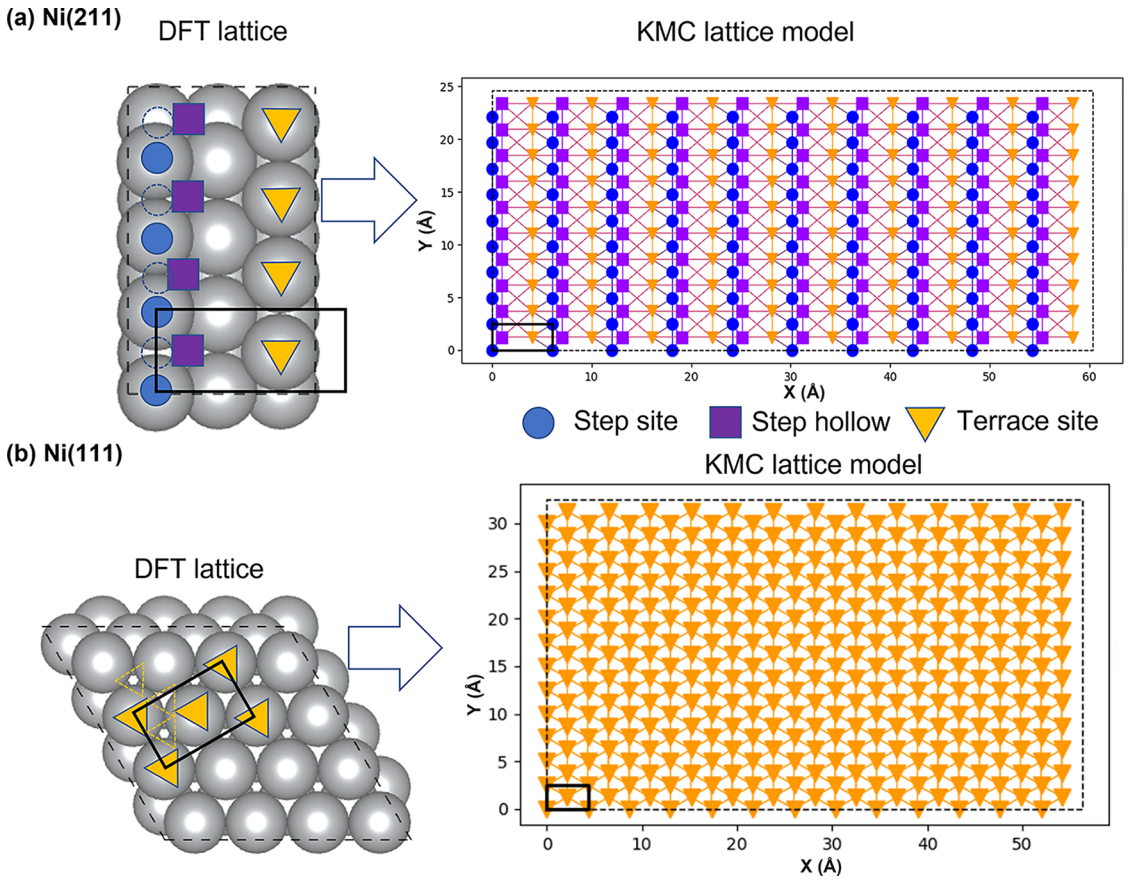

Figure 1. The DFT lattice and KMC lattice model used in this study. (a) Top view of the Ni(211) surface (left), where different symbols represent three distinct adsorption sites: step, step-hollow, and terrace. Dashed circles indicate step-bridge sites, which are coarse-grained into step sites (solid circles). The dashed parallelogram outlines the DFT surface unit cell, while the solid parallelogram indicates the KMC lattice unit cell. The corresponding KMC lattice model is shown on the right. (b) Top view of the Ni(111) surface (left) and the corresponding KMC lattice model (right). Terrace bridge sites and hcp/fcc hollow sites, shown as dashed triangles in the atomistic model, are coarse-grained into terrace sites (solid triangles) in the KMC lattice. The dashed outline indicates the DFT surface unit cell, while the solid outline indicates the KMC lattice unit cell.

the harmonic oscillator model was employed to estimate the relevant partition functions.

The preparation, data analysis, and visualization of the KMC simulations were carried out using ZacrosTools.[41] In contrast to traditional MKM models, on-lattice KMC models retain the spatial information on site connectivity, adsorbate lateral interactions, and spatial correlation effects. Based on the DFT results, the stable adsorption sites for MSR species on Ni(211) are the step-top, step-bridge, and the four-fold step-hollow. For simplification, the step-top and step-bridge sites are grouped together as a single "step site" in the KMC model, as shown in Figure 1a. Similarly, on Ni(111), reactions occurring at either bridge or hollow sites are treated as occurring on a single "terrace site." Additionally, the terrace sites on Ni(211) are assumed to exhibit identical energetics and reactivity as those on Ni(111). Accordingly, in the stepped-surface KMC models, terrace-site reactions and energetics are taken from the Ni(111) dataset, whereas step-site reactions and energetics are taken from the Ni(211) dataset. Thus, the Ni(211), Ni(533), and Ni(11 9 9) models all combine Ni(211)-based step chemistry with Ni(111)-based terrace chemistry. The difference among these stepped models lies in the density and geometric arrangement of step and terrace sites in the lattice.

As a result, the Ni(211) KMC unit cell includes three distinct site types: step site, step-hollow site, and terrace site, while the Ni(111) KMC model contains only the terrace site. Repeating the unit cell 10 × 10 times for Ni(211) and 13 × 13 times for Ni(111) yields lattices with 300 and 338 sites, respectively, as shown in Figure 1.

The MSR reaction network is depicted in Figure 2 , while the detailed list of the 74 reversible elementary processes is provided in Tables S1 and S5. Specifically, Table S1 contains the gas-surface and surface reaction steps, whereas Table S5 lists the diffusion events, giving a total of 10 adsorption/desorption steps, 26 surface reactions, and 38 diffusion steps.

Since the MSR reaction network features numerous adsorbates, the number of possible adsorbate-adsorbate interaction terms (patterns) can be very large, but not all such patterns would be relevant in the KMC simulations. Thus, to keep the KMC models simple yet relevant, the following interactions were accounted for: (1) pairwise interactions between species involved in a bimolecular reaction; (2) lateral interactions among high-coverage species; and (3) interactions between pairs of adsorbates—often involving high- and low-coverage species—that appeared frequently in preliminary simulations. As a result, the energetics model incorporates 29 one-body terms (refer to Table S3) and 115 two-body terms (refer to Table S4). In *Zacros*, the influence of lateral interactions on energy barriers is handled using the Brønsted-Evans-Polanyi relations which are linear expressions of the activation energy and the energy of reaction in the presence of spectators.[22,42]

For the MSR reaction on each facet, we evaluated the turnover frequency (TOF) for all possible products (H_2, CO and CO_2), as well as selectivity and site-specific adsorbate coverage, over a wide range of temperatures (600–1300 K) and total pressures (0.01–10 bar) at a specified methane-to-water ratio. These results were visualized as heat maps by sampling the temperature linearly and the pressure

https://doi.org/10.1021/acscatal.6c01172
ACS Catal. XXXX, XXX, XXX–XXX

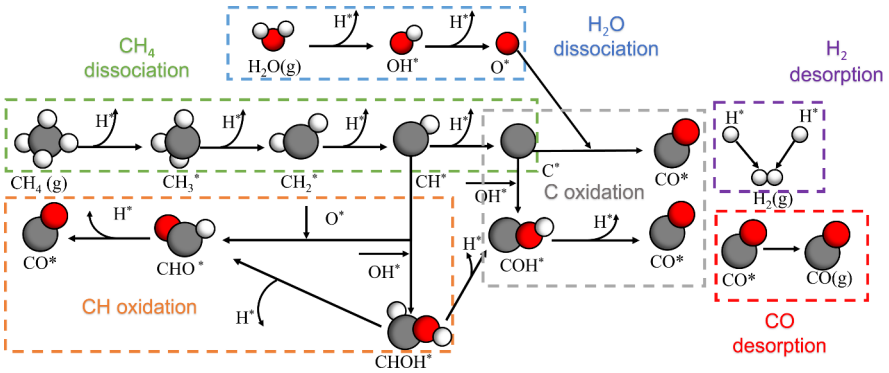

Figure 2. The key elementary events of MSR on Ni surfaces. CO_2 formation is excluded since it is a side reaction in the MSR reaction network.

logarithmically in a 10 × 10 grid (i.e., 100 KMC simulations per methane-water ratio on each facet). To address the time-scale disparity problem in KMC, we employed a dynamic scaling algorithm that accelerates the simulation on the fly. Additionally, we raised to 0.40 eV the energy barriers for all symmetric diffusion steps that had barriers below 0.40 eV. Tests verified that this adjustment does not alter the simulation results apart from enabling a faster approach to steady state.[43] Each KMC simulation was conducted for up to 72 h of real time or until 50,000 s of simulated time was reached, whichever occurred first. To confirm that all simulations had attained steady-state (stationary) conditions, ZacrosTools implements a dedicated function that automates this task, which was employed in our studies (see Note S1 in the Supporting Information for additional details on this procedure and the parameters used in the dynamic scaling algorithm). Due to the large number of KMC simulations required for this study, only a single simulation was carried out for each set of operating conditions (water pressure, methane pressure, and temperature). Nevertheless, in view of the long KMC times attained and the rigorous detection of steady-state conditions, conducting multiple replicas for each parameter set is not necessary.

3. RESULTS AND DISCUSSION

3.1. MSR Pathways on Ni(111) and Ni(211)

We start by systematically comparing the DFT-predicted energy barriers for the MSR elementary events on the Ni(211) and Ni(111) surfaces. As illustrated in Figure 3, the Ni(211) surface exhibits higher reactivity for most elementary steps, notably including methane activation—commonly regarded as the rate-determining step of MSR at certain conditions.[44,45] Note though that these observations are based on just the activation barriers; kinetic simulations are subject to additional effects, e.g. availability of reactive intermediates on the surface and coverage effects, which may alter these trends. Nevertheless, the trends emerging from Figure 3 align with expectations of the behavior of stepped surfaces, where the undercoordinated sites would facilitate bond cleavage. A particularly striking example is the CH dissociation step, which has a substantially lower energy barrier on Ni(211) (0.72 eV) than on Ni(111) (1.31 eV), potentially exacerbating catalyst poisoning due to facile carbon formation. In contrast, formation and dissociation of CHOH follow the opposite trend, demonstrating higher barriers on Ni(211).

This pattern is consistent with earlier reports on dry methane reforming,[46] which proceeds through a mechanism similar to that of MSR. Generally, Ni(211) lowers the energy barriers for most steps, with the notable exception of CHOH formation/dissociation. Four main competing pathways contribute to CO generation: (i) direct C* oxidation, which has relatively large activation energies (1.74 eV on Ni(211), 2.28 eV on Ni(111)) and thus likely becomes significant only at elevated temperatures; (ii) CHO-mediated CO formation, involving CH* + O* to form CHO* (1.44 eV on Ni(211), 1.51 eV on Ni(111)) followed by facile CH bond cleavage towards CO and H (0.05 eV on Ni(211), 0.18 eV on Ni(111)); (iii) a COH-mediated route requiring two steps—formation of COH* by oxidizing C* with OH* (1.82 eV on Ni(211), 1.41 eV on Ni(111)), then OH bond cleavage to produce CO (0.49 eV on Ni(211), 0.91 eV on Ni(111)); and (iv) the CHOH pathway, whereby CH* and OH* species react to form CHOH* (2.17 eV on Ni(211), 1.45 eV on Ni(111)), which undergoes O–H/C–H bond dissociations to yield CHO*/COH* intermediates. Notably, Ni(211) favors the C oxidation pathway, whereas Ni(111) favors pathways proceeding via the CHOH intermediate. Because of these competing pathways, identifying a single dominant CO forming route solely from DFT-predicted energy barriers is not straightforward. Moreover, as noted earlier the DFT model does not account for coverage effects, which strongly influence MSR kinetics. Thus, a KMC model is required to establish the dominant reforming pathway(s) under realistic MSR operating conditions.

3.2. Kinetic Modelling of MSR

3.2.1. Activity and Selectivity Trends. We proceed by comparing the KMC simulation results for MSR on Ni(211) and Ni(111) under industrially relevant conditions, which include temperatures ranging from 600 to 1300 K, total pressure varying from 0.01 to 10 bar, and a reactant molar ratio of CH_4:H_2O = 1:3 in the feed. As shown in Figure 4, the highest TOFs are obtained at the highest values of temperature and pressure (1300 K and 10 bar), which is in line with the industrial operating conditions.[18] The KMC-predicted TOFs deviate significantly from the trends suggested by DFT-based energy barrier comparisons alone. According to the DFT predictions, Ni(211) should exhibit higher reactivity due to its lower activation energies for most elementary steps. However, as shown in Figure 4a,b, the H_2 turnover rates of Ni(211) predicted by KMC are consistently lower than those of Ni(111) at high temperatures and pressures.

This discrepancy can be attributed to coverage effects, particularly surface poisoning. As shown in Figure 4b, on Ni(211), extensive poisoning (high species coverages) is observed

https://doi.org/10.1021/acscatal.6c01172
ACS Catal. XXXX, XXX, XXX–XXX

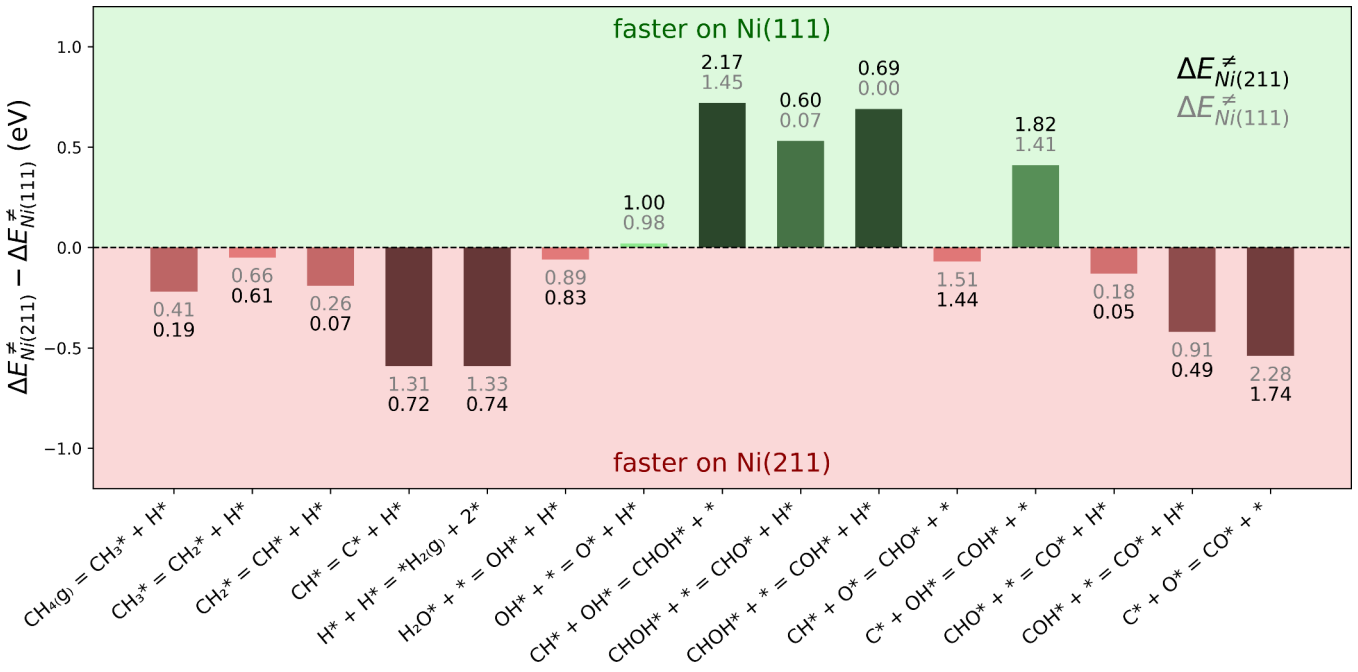

Figure 3. The difference in the energy barriers for the MSR elementary steps between Ni(211) ($\Delta E^{\neq}_{Ni(211)}$) and Ni(111) ($\Delta E^{\neq}_{Ni(111)}$). Values shown above or below each bar correspond to the barriers on Ni(211) (black) and Ni(111) (gray), respectively. The bar color indicates whether the barrier difference is positive or negative, with green representing positive values and red representing negative values, while the color intensity reflects the magnitude of this difference. All barrier values are in electron volts (eV) and exclude zero-point energy contributions. For cases with two reactants, the barriers are calculated from an initial state where the reactants are infinitely separated (i.e., no lateral interaction). The symbol "*" indicates an empty site, and a species labeled with "*" in the superscript is an adsorbate on the Ni surface, while "(g)" denotes gas phase species.

regardless of operating conditions. The step hollow sites are heavily occupied by carbon species (~50%), while step sites suffer from CH* poisoning, reaching over 60% coverage at low temperatures, with this poisoning effect only partially alleviated at higher temperatures. Terrace sites also experience significant poisoning by CH* under low-temperature/high-pressure conditions and by C* at high temperatures/low pressures, as shown in the coverage and phase diagrams of Figure 4a. In contrast, Ni(111) maintains significantly lower levels of poisoning (less than 40% above 800 K), thereby exhibiting sustained catalytic activity (refer to Figure 4a). The origin of this poisoning lies in the high C-H bond cleavage activity on Ni(211), which promotes rapid accumulation of CH* and C* species—especially at step sites—ultimately blocking access to active centers and limiting the overall reaction rate. Despite the TOFs of H_2 on Ni(211) being lower than those on Ni(111), the former surface is predicted by KMC to exhibit better selectivity towards CO. Indeed, the heat maps show that CO_2 is not produced on Ni(211) but is generated on Ni(111) under a broad range of conditions. This can be explained by the prohibitively high barrier (3.90 eV) for CO* and O* to form CO_2 on Ni(211); on the contrary, the barrier for this reaction is much lower (1.62 eV) on Ni(111).

Furthermore, the comparison of TOF trends between two facets shows distinct sensitivities: Ni(111) exhibits a stronger dependence on partial pressure, while Ni(211) displays more pronounced temperature dependence. This behavior is quantified in Figure 5a using Spearman correlation coefficients (detailed equations are shown in Note S2 in the SI), which measure the strength and direction of monotonic relationships between variables. The analysis reveals that temperature plays an important role in determining the TOFs on both surfaces, with Ni(211) showing greater sensitivity to temperature changes. In contrast, the partial pressure of CH_4 exerts a stronger positive influence on the TOFs of both H_2 and CO on Ni(111) than on Ni(211), whereas the partial pressure of H_2O has a more pronounced effect on the CO and H_2 TOFs in the Ni(211) system compared to Ni(111).

To explain these trends, we note that Ni(111) exhibits water-induced surface poisoning at low temperatures, suggesting a saturation effect and a limited ability to dissociate H_2O under such conditions. Although the activation energy barriers for water dissociation are similar on both surfaces, the water adsorption energy on the undercoordinated step sites of Ni(211) is much lower than that on Ni(111) (as shown on Table S1), indicating that Ni(211) has a greater capacity for water adsorption (more negative adsorption energy means greater stability, as per the convention used herein). Indeed, Figure 5b,c show that, under high-pressure conditions, both the Ni(211) step and terrace sites are active for water adsorption and dissociation, with the step site showing slightly higher activity. This distinction becomes particularly evident when evaluating the effect of varying the CH_4:H_2O feed ratio. As shown in Figure 6, increasing the partial pressure of water leads to a marked improvement in the H_2 TOF on Ni(211), eventually surpassing the performance of Ni(111). This trend highlights the superior water dissociation capability of Ni(211), which compensates for its carbon poisoning under specific operating conditions and enables enhanced H_2 production at higher steam concentrations.

3.2.2. Dominant Pathways. We have analyzed the dominant MSR pathways at 1300 K and 10 bar (this point lies within

https://doi.org/10.1021/acscatal.6c01172
ACS Catal. XXXX, XXX, XXX–XXX

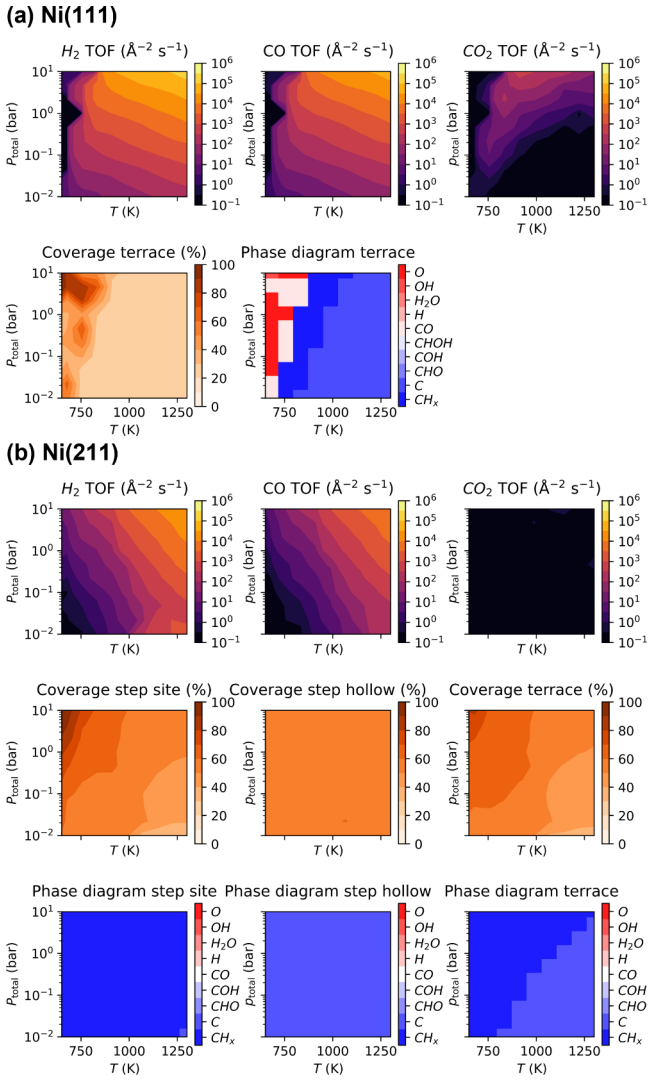

Figure 4. The heat maps for turnover frequencies, coverages, and dominant species for (a) Ni(111) and (b) Ni(211) at a reactant feed ratio of CH_4:H_2O = 1:3. The first row shows TOFs of the products, and the second row shows the total coverages on different sites over a large range of temperatures and pressures. Finally, the phase diagram shows the dominant species on the surface.

the operating condition range of MSR) for varying CH_4–H_2O ratios, and the results are summarized in Figure 7. Ni(111) exhibits a higher overall reforming rate under low water partial pressure conditions, whereas Ni(211) outperforms Ni(111) at CH_4:H_2O = 1:7, where no reforming reaction occurs on Ni(111) due to severe surface poisoning by oxygen and OH species. Increasing the partial pressure of water enhances the performance of both surfaces. Notably, Ni(211) shows a significant improvement at CH_4:H_2O = 1:10, which is consistent with its strong water dissociation capability.

As discussed previously, DFT calculations of Ni(211) show that the CHO-mediated route has the lowest energy barrier, followed by direct CO formation (C* + O* → CO*), and finally the COH pathway. In contrast, the KMC flux analysis shows that oxidation pathways that consume C* are favorable, namely direct CO formation and the COH route. As shown in Figure 7a, at CH_4:H_2O = 1:1, the COH pathway is predominant. The decomposition of the Ni(211) contributions further shows that CO and COH formation are mainly associated with step sites, whereas CHOH formation and most of the CHO formation contribution originate from terrace sites. For higher water partial pressures, the dominant pathway shifts toward direct CO formation, and at a ratio of 1:5, the contribution of the CHO pathway to the total rate surpasses that of the COH pathway. This is because higher water partial pressure leads to increased O* coverage on the surface, which promotes both the CO and CHO pathways. For Ni(111), the DFT predicted energy barriers for the CHO and COH pathways are comparable, whereas direct CO formation is significantly less favorable energetically. Coverage plots on Figure 4 reveal that CH* dominates the surface below ∼1000 K, indicating sluggish oxidation thereof at low temperatures. At higher temperatures, CH* coverage decreases sharply, and the CHO pathway becomes more dominant. Under the examined conditions, the CHO route remains the primary oxidation pathway on Ni(111), followed by the COH pathway. This result is consistent with previous studies.[47] The CHOH-mediated pathway is essentially inactive on both facets. On Ni(211), the forward barrier for CHOH formation is prohibitively high, while in the case of Ni(111), even though this species can form, the reverse barrier is only 0.51 eV, causing CHOH* to rapidly dissociate back to CH* + OH* immediately after formation. As a result, the conversion of CHOH* into either CHO* or COH* is exceedingly rare. The oxidation pathway analysis shows that Ni(111) exhibits better resistance to poisoning, as the rate of carbon removal steps is significantly higher than on Ni(211). This explains the high carbon coverage observed on Ni(211), which results from the combined effects of its high CH* dissociation rate and relatively low reforming activity.

3.2.3. Optimization of Operating Conditions. Given that the reactivities of Ni(211) and Ni(111) exhibit different sensitivities to the partial pressures of the two reactants, it is of particular interest to determine the conditions under which each surface achieves its highest TOF. To explore this, additional sets of KMC simulations were performed at 1300 K, for a range of partial pressures of CH_4 and H_2O. As shown in Figure 8, Ni(211) exhibits a maximum TOF for $P(H_2O)$ = 10 bar and $P(CH_4)$ = 0.8 to 1.0 bar within the range of partial pressures investigated. This suggests that, for a surface composed purely of repeating step sites, the optimal feed ratio is CH_4:H_2O = 1:10, owing to the favorable adsorption and dissociation capabilities of the step sites. In contrast, Ni(111) shows a maximum TOF (for the parameter region investigated) within the range of $P(H_2O)$ = 10 bar and $P(CH_4)$ = 2.1 to 4.6 bar, indicating an optimal feed ratio of CH_4:H_2O = 1:3 to 1:5. Notably, this is consistent with typical industrial operating conditions.[2] In line with this, experimental studies on industrial Ni-based catalysts have reported a clear dependence of carbon formation on the steam-to-methane ratio, with more severe carbon deposition observed at lower steam contents.[48]

Since step sites are susceptible to poisoning and exhibit lower DFT energy barriers for most of the elementary steps of MSR, we varied the step site density to mimic realistic nanoparticle surfaces, characterized by different step:terrace site ratios depending on size, and assessed the significance of step sites. Figure 9 shows the H_2 TOF and surface coverage of terrace site of two representative cases: (i) Ni(533) which has 2 more terrace sites than (211) in the unit cell and contains total number of 320 sites in its lattice model (ii) Ni(11 9 9) which has 8 more

https://doi.org/10.1021/acscatal.6c01172
ACS Catal. XXXX, XXX, XXX–XXX

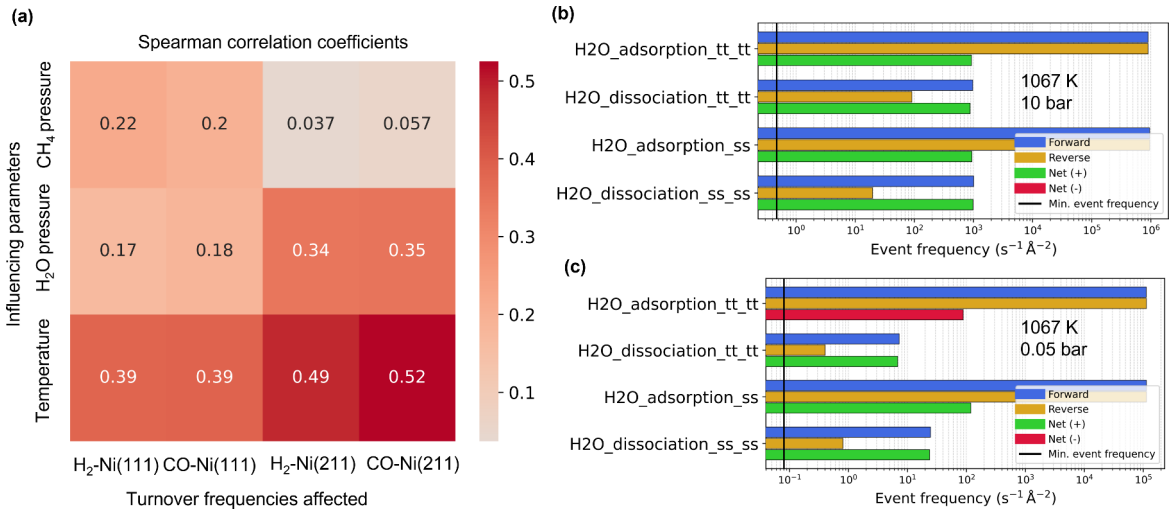

Figure 5. (a) Spearman correlation coefficients for TOFs on Ni(211) and Ni(111) as a function of temperature and partial pressures. Higher values indicate a stronger monotonic trend between the TOF and the influencing variable. (b) Process statistics of water-involving reactions on Ni(211) at 1067 K and 10 bar. The labels "tt" and "ss" indicate that the elementary step occurs on terrace and step sites, respectively. (c) Same as in panel (b), but at a lower total pressure of 0.05 bar.

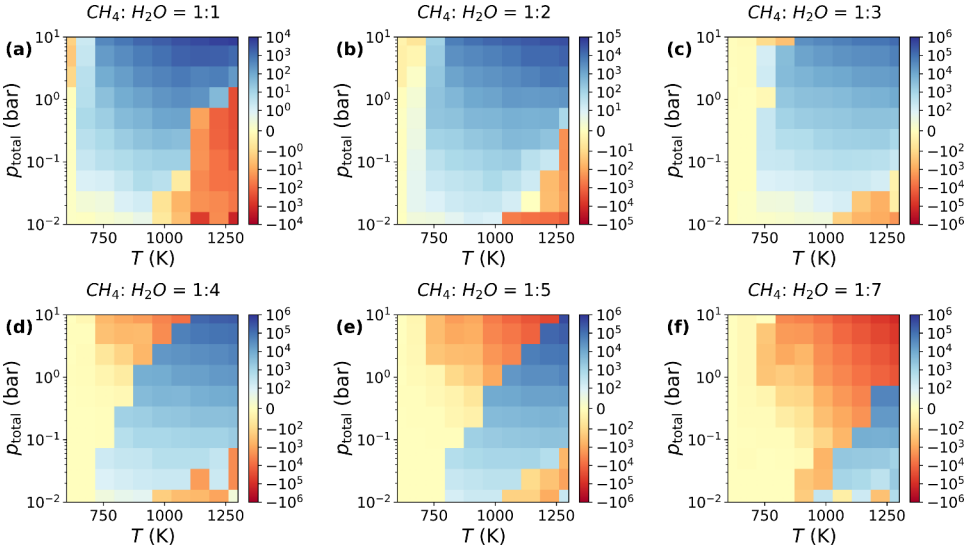

Figure 6. Differences in the TOF of H_2 between Ni(111) and Ni(211) surfaces for the following CH_4:H_2O gas feed ratios: (a) 1:1, (b) 1:2, (c) 1:3, (d) 1:4, (e) 1:5, (f) 1:7. Blue indicates Ni(111) has better TOF, while red indicates Ni(211) has better performance. As the partial pressure of water is increased, the H_2 TOF of Ni(211) becomes larger than that of Ni(111).

repeated terrace sites in the unit cell and contains total number of 275 sites in its lattice model (detailed lattice models and coverages of other two types of sites can be found in Figures S2 and S3). Both of the KMC simulations are performed at 1300 K, 10 bar, and a CH_4:H_2O ratio of 1:3. The results indicate that increasing the number of step sites leads to reduced TOFs and more severe poisoning, in good agreement with previous theoretical and experimental studies,[6,11,49] which have focused either on imaging individual particles or on local energetics at idealized step and terrace sites. Our results also reveal that carbon formed at steps can diffuse onto neighboring terraces and poison them, explaining the increase in terrace carbon coverage in the presence of step sites on the surface. Since coke formation is not treated explicitly in the model, the results presented are relevant to the early stages of the reaction, during which coke precursors are emerging but have not yet started coupling towards graphene-type islands. Ongoing research in our lab is focusing on the subsequent coking chemistry, which presents significant challenges due to the complexity of the underlying pathways.

4. CONCLUSIONS

Although the MSR reaction on Ni surfaces has been widely investigated, the effect of Ni step sites on the MSR kinetics is not well understood. In this work, we elucidate the effect of these sites by using Ni(211) as a model surface and drawing comparisons against the Ni(111) surface. DFT calculations

https://doi.org/10.1021/acscatal.6c01172
ACS Catal. XXXX, XXX, XXX−XXX

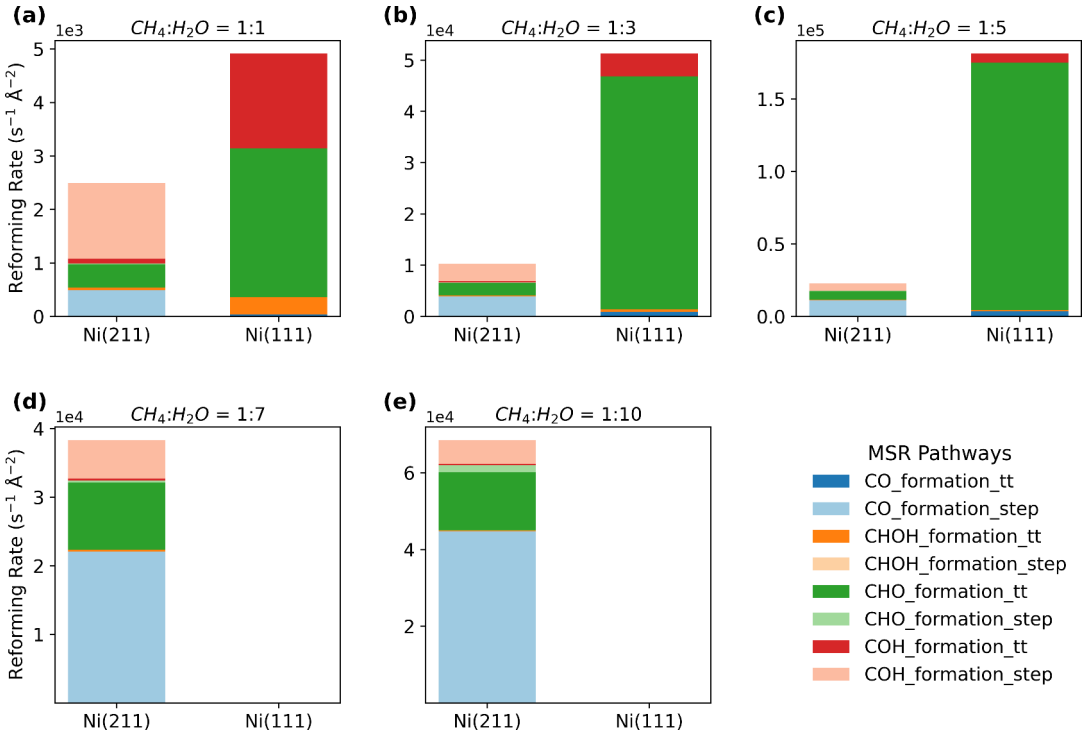

Figure 7. The contributions of MSR reforming pathways on Ni(211) and Ni(111) surfaces. The net reforming rates associated with different elementary pathways (CO, CHOH, CHO, and COH formation) are shown as stacked bar plots for both surfaces under varying CH_4:H_2O ratios. Panels (a)–(e) correspond to increasing H_2O partial pressure (from CH_4:H_2O = 1:1 to 1:10), at 1300 K and a total pressure of 10 bar. The contributions on Ni(211) are further decomposed into terrace-site contributions (dark colors) and step-site contributions (light colors).

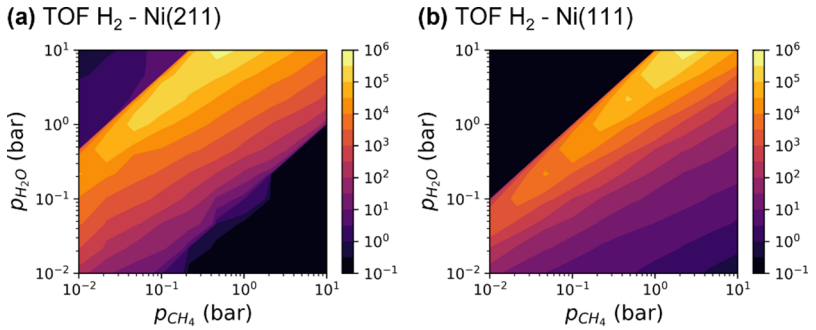

Figure 8. Heat maps of H_2 TOF over a range of partial pressures of CH_4 and H_2O at 1300 K, for (a) Ni(211) and (b) Ni(111).

show that Ni(211) is more reactive for most MSR elementary steps. However, KMC simulations that explicitly include both step and terrace sites and the full MSR reaction network reveal that the H_2 TOFs on Ni(211) are lower than those on Ni(111) at industrial operating conditions, primarily due to carbon poisoning. To further understand this behavior, we conducted high-throughput KMC simulations over a broad range of conditions—varying the partial pressures of water and methane, as well as the temperature. The results show that the TOF of Ni(211) is more sensitive to water partial pressure and temperature, while for Ni(111) the parameters with the strongest influence on TOF are methane partial pressure and temperature. The KMC flux analysis at different operating conditions indicates that Ni(111) exhibits better resistance to coking than Ni(211). Additionally, we performed partial pressure scans for both surfaces and identified their optimal operating conditions. Finally, our detailed lattice KMC model, which, in addition to the MSR chemistry takes into account the diffusion of strongly bound carbonaceous precursors over the entire surface, enabled us to investigate the effect of the step site density on the MSR kinetics under industrially relevant conditions. We thus found that increasing the number of step sites reduces the overall TOF and enhances surface poisoning, in agreement with the previously established experimental picture that steps are preferred coking centers. Crucially, our simulations went beyond the previous work by providing a direct, site-resolved link between step density, TOF, and carbon species coverage.

This work provides a deeper insight into the mechanism by which step sites influence the kinetics of MSR, and demonstrates that KMC simulation is a powerful tool for evaluating

https://doi.org/10.1021/acscatal.6c01172
ACS Catal. XXXX, XXX, XXX–XXX

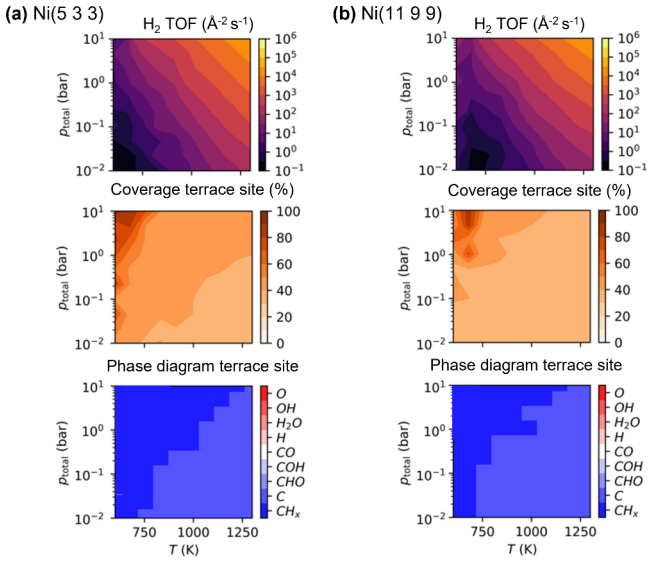

Figure 9. The heat map of (a) Ni(533) and (b) Ni(11 9 9) at a reactant feed ratio of CH_4:H_2O = 1:3.

catalytic performance. More specifically, the present lattice KMC treatment shows that step sites are not always enhancing surface reactivity; their presence can become detrimental under working conditions because they promote local poisoning and reduce the population of kinetically productive sites. By explicitly resolving the local surface environment that develops dynamically under reaction conditions, the present KMC approach goes beyond previous mean-field treatments and provides a more realistic understanding of how different active surfaces perform, thereby aiding catalyst design and reaction-condition optimization.

Future research efforts could focus on incorporating carbon growth mechanisms—such as the formation of carbon chains, carbon rings, or complex C_xH_y structures—into the KMC models. This extension could simulate the nucleation process of carbon whiskers and provide a more comprehensive understanding of the coking and poisoning mechanisms. In addition, a more complete analysis of the water-gas shift (WGS) reaction under steam reforming conditions would require an expanded reaction network including the missing CO_2-related elementary steps and key intermediates, such as COOH*, HCOO*, and their associated hydrogenation/dehydrogenation reactions, which are beyond the scope of the present MSR-focused model. Moreover, with a detailed model of carbon growth and a more complete treatment of WGS chemistry, it would then be possible to identify next-generation Ni-based catalysts (such as single-atom alloy, bimetallic, and trimetallic catalysts) that exhibit high activity and stability.

■ ASSOCIATED CONTENT

Supporting Information

The Supporting Information is available free of charge at https://pubs.acs.org/doi/10.1021/acscatal.6c01172.

Table S1: List of steps included in the KMC models, along with the calculated forward energy barrier, reverse energy barrier, and reaction energy for each step; Table S2: DFT formation energies (in eV) of adsorbed species; Table S3: DFT formation energies (in eV) of the gas-phase molecules; Table S4: lateral interaction energies; Table S5: diffusion events included in the KMC models; Figure S1: the potential energy surface of MSR reactions on the Ni(211) surface; Figures S2 and S3: KMC lattice models and heat maps for the TOF, total coverage, and dominant species (phase diagram) for Ni(533) and Ni(11 9 9), respectively; Figure S4: tests for convergence with respect to lattice size for the Ni(211) model; Note S1: procedure for ensuring that the steady-state is reached in all KMC simulations; Note S2: calculation of Spearman correlation coefficients; and Note S3: methodology for pathway contribution analysis (PDF)

■ AUTHOR INFORMATION

Corresponding Author

Michail Stamatakis – *Inorganic Chemistry Lab, Department of Chemistry, University of Oxford, Oxford OX1 3QR, U.K.*; orcid.org/0000-0001-8338-8706; Email: michail.stamatakis@chem.ox.ac.uk

Authors

Zeyu Wu – *Inorganic Chemistry Lab, Department of Chemistry, University of Oxford, Oxford OX1 3QR, U.K.*

Sai Sharath Yadavalli – *Inorganic Chemistry Lab, Department of Chemistry, University of Oxford, Oxford OX1 3QR, U.K.*

Carlos Fonte – *Johnson Matthey Technology Centre, Blount's Court Sonning Common, Reading RG4 9NH, U.K.*

Complete contact information is available at: https://pubs.acs.org/doi/10.1021/acscatal.6c01172

Notes

The authors declare no competing financial interest.

■ ACKNOWLEDGMENTS

Z.W.'s doctoral studies are supported by an Impact Studentship sponsored by the Johnson Matthey Davy Technologies Limited. We gratefully acknowledge the use of the following computing facilities for the simulations of this work: the Oxford Advanced Research Computing (ARC) Facility; the Hydra cluster at Oxford Chemistry, the hardware of which was sponsored by the John Fell Oxford University Press (OUP) Research Fund (application #0015331); and the HPC facility Young by the U.K. Materials and Molecular Modelling Hub, which is partially funded by EPSRC (EP/T022213/1, EP/W032260/1, and EP/P020194/1). Finally, we would like to thank Dr. Hector Prats for helpful discussions.

■ REFERENCES

(1) Luo, Y.; Guan, Y.; Liu, G.; et al. First-Principles-Based Kinetic Monte Carlo Model of Hydrogen Evolution Reaction under Realistic Conditions: Solvent, Hydrogen Coverage and Electric Field Effects. *ACS Catal.* **2024**, *14* (4), 2696–2708.

(2) Blaylock, D. W.; Ogura, T.; Green, W. H.; et al. Computational Investigation of Thermochemistry and Kinetics of Steam Methane Reforming on Ni(111) under Realistic Conditions. *J. Phys. Chem. C* **2009**, *113* (12), 4898–4908.

(3) Ishaq, H.; Dincer, I.; Crawford, C. A review on hydrogen production and utilization: Challenges and opportunities. *Int. J. Hydrogen Energy* **2022**, *47* (62), 26238–26264.

(4) Salhi, N.; Boulahouache, A.; Petit, C.; et al. Steam reforming of methane to syngas over $NiAl_2O_4$ spinel catalysts. *Int. J. Hydrogen Energy* **2011**, *36* (17), 11433–11439.
(5) Sikiru, S.; Oladosu, T. L.; Amosa, T. I.; et al. Hydrogen-powered horizons: Transformative technologies in clean energy generation, distribution, and storage for sustainable innovation. *Int. J. Hydrogen Energy* **2024**, *56*, 1152–1182.
(6) Bengaard, H. S.; Nørskov, J. K.; Sehested, J.; et al. Steam Reforming and Graphite Formation on Ni Catalysts. *J. Catal.* **2002**, *209* (2), 365–384.
(7) Mohan, O.; Shambhawi; Lapkin, A. A.; et al. Investigating methane dry reforming on Ni and B promoted Ni surfaces: DFT assisted microkinetic analysis and addressing the coking problem. *Catal. Sci. Technol.* **2020**, *10* (19), 6628–6643.
(8) Meloni, E.; Martino, M.; Palma, V. A Short Review on Ni Based Catalysts and Related Engineering Issues for Methane Steam Reforming. *Catalysts* **2020**, *10* (3), 352.
(9) Wang, H.; Blaylock, D. W.; Dam, A. H.; et al. Steam methane reforming on a Ni-based bimetallic catalyst: density functional theory and experimental studies of the catalytic consequence of surface alloying of Ni with Ag. *Cat. Sci. Technol.* **2017**, *7* (8), 1713–1725.
(10) Sehested, J. Four challenges for nickel steam-reforming catalysts. *Catal. Today* **2006**, *111* (1-2), 103–110.
(11) Helveg, S.; Lopez-Cartes, C.; Sehested, J.; et al. Atomic-scale imaging of carbon nanofibre growth. *Nature* **2004**, *427* (6973), 426–429.
(12) Jiang, B.; Liu, R.; Li, J.; et al. Mode selectivity in methane dissociative chemisorption on Ni(111). *Chem. Sci.* **2013**, *4* (8), 3249–3254.
(13) Salcedo, A.; Lustemberg, P. G.; Rui, N.; et al. Reaction Pathway for Coke-Free Methane Steam Reforming on a Ni/CeO_2 Catalyst: Active Sites and the Role of Metal-Support Interactions. *ACS Catal.* **2021**, *11* (13), 8327–8337.
(14) Delgado, K.; Maier, L.; Tischer, S.; et al. Surface Reaction Kinetics of Steam- and CO_2-Reforming as Well as Oxidation of Methane over Nickel-Based Catalysts. *Catalysts* **2015**, *5* (2), 871–904.
(15) Guo, D.; Li, M.; Lu, Y.; et al. Enhanced Thermocatalytic Stability by Coupling Nickel Step Sites with Nitrogen Heteroatoms for Dry Reforming of Methane. *ACS Catal.* **2021**, *12* (1), 316–330.
(16) Saadi, S.; Abild-Pedersen, F.; Helveg, S.; et al. On the Role of Metal Step-Edges in Graphene Growth. *J. Phys. Chem. C.* **2010**, *114* (25), 11221–11227.
(17) Lozano-Reis, P.; Prats, H.; Sayós, R.; et al. Limitations of free energy diagrams to predict the catalytic activity: The reverse water gas shift reaction catalyzed by Ni/TiC. *J. Catal.* **2023**, *425*, 203–211.
(18) Blaylock, D. W.; Zhu, Y.-A.; Green, W. H. Computational Investigation of the Thermochemistry and Kinetics of Steam Methane Reforming Over a Multi-Faceted Nickel Catalyst. *Top. Catal.* **2011**, *54* (13-15), 828–844.
(19) Gracia, A.; Lozano-Reis, P.; Huarte-Larrañaga, F.; et al. CO_2 hydrogenation on Ni(111): microkinetic modelling vs kinetic Monte Carlo simulations – choosing the right approach for unravelling reaction kinetics. *RSC Sustainability* **2025**, *3* (8), 3499–3512.
(20) Ravipati, S.; d'Avezac, M.; Nielsen, J. et al. A Caching Scheme To Accelerate Kinetic Monte Carlo Simulations of Catalytic Reactions. *J. Phys. Chem. A.* **2020**, *124* (35), 7140–7154.
(21) Stamatakis, M.; Vlachos, D. G. A graph-theoretical kinetic Monte Carlo framework for on-lattice chemical kinetics. *J. Chem. Phys.* **2011**, *134* (21), No. 214115.
(22) Nielsen, J.; d'Avezac, M.; Hetherington, J. et al. Parallel kinetic Monte Carlo simulation framework incorporating accurate models of adsorbate lateral interactions. *J. Chem. Phys.* **2013**, *139* (22), No. 224706.
(23) Benson, R. L.; Yadavalli, S. S.; Stamatakis, M. Speeding up the Detection of Adsorbate Lateral Interactions in Graph-Theoretical Kinetic Monte Carlo Simulations. *J. Phys. Chem. A.* **2023**, *127* (48), 10307–10319.
(24) Kresse, G.; Hafner, J. Ab initio molecular-dynamics simulation of the liquid-metal-amorphous-semiconductor transition in germanium. *Phys. Rev. B.* **1994**, *49* (20), 14251–14269.
(25) Kresse, G.; Furthmüller, J. Efficient iterative schemes for ab initio total-energy calculations using a plane-wave basis set. *Phys. Rev. B.* **1996**, *54* (16), 11169–11186.
(26) Kresse, G.; Furthmüller, J. Efficiency of ab-initio total energy calculations for metals and semiconductors using a plane-wave basis set. *Comput. Mater. Sci.* **1996**, *6* (1), 15–50.
(27) Grimme, S.; Ehrlich, S.; Goerigk, L. Effect of the damping function in dispersion corrected density functional theory. *J. Comput. Chem.* **2011**, *32* (7), 1456–1465.
(28) Yadavalli, S. S.; Jones, G.; Stamatakis, M. DFT benchmark studies on representative species and poisons of methane steam reforming on Ni(111). *Phys. Chem. Chem. Phys.* **2021**, *23* (29), 15601–15612.
(29) Makov, G.; Payne, M. C. Periodic boundary conditions in ab initio calculations. *Phys. Rev. B.* **1995**, *51* (7), 4014–4022.
(30) Kresse, G.; Joubert, D. From ultrasoft pseudopotentials to the projector augmented-wave method. *Phys. Rev. B.* **1999**, *59* (3), 1758–1775.
(31) Monkhorst, H. J.; Pack, J. D. Special points for Brillouin-zone integrations. *Phys. Rev. B.* **1976**, *13* (12), 5188–5192.
(32) Garrido Torres, J. A.; Jennings, P. C.; Hansen, M. H.; et al. Low-Scaling Algorithm for Nudged Elastic Band Calculations Using a Surrogate Machine Learning Model. *Phys. Rev. Lett.* **2019**, *122* (15), No. 156001.
(33) Hansen, M. H.; Garrido Torres, J. A.; Jennings, P.; et al. An Atomistic Machine Learning Package for Surface Science and Catalysis. *arXiv* **2019**.
(34) Henkelman, G.; Uberuaga, B. P.; Jónsson, H. A climbing image nudged elastic band method for finding saddle points and minimum energy paths. *J. Chem. Phys.* **2000**, *113* (22), 9901–9904.
(35) Henkelman, G.; Jónsson, H. A dimer method for finding saddle points on high dimensional potential surfaces using only first derivatives. *J. Chem. Phys.* **1999**, *111* (15), 7010–7022.
(36) Hafner, J. Ab-initio simulations of materials using VASP: Density-functional theory and beyond. *J. Comput. Chem.* **2008**, *29* (13), 2044–2078.
(37) Jain, A.; Hautier, G.; Moore, C. J.; et al. A high-throughput infrastructure for density functional theory calculations. *Comput. Mater. Sci.* **2011**, *50* (8), 2295–2310.
(38) Hjorth Larsen, A.; Jorgen Mortensen, J.; Blomqvist, J.; et al. The atomic simulation environment-a Python library for working with atoms. *J. Phys. Condens. Matter* **2017**, *29* (27), No. 273002.
(39) Yadavalli, S. S.; Jones, G.; Benson, R. L. et al. Assessing the Impact of Adlayer Description Fidelity on Theoretical Predictions of Coking on Ni(111) at Steam Reforming Conditions. *J. Phys. Chem. C* **2023**, *127* (18), 8591–8606.
(40) Stamatakis, M.; Vlachos, D. G. Unraveling the Complexity of Catalytic Reactions via Kinetic Monte Carlo Simulation: Current Status and Frontiers. *ACS Catal.* **2012**, *2* (12), 2648–2663.
(41) Prats, H. ZacrosTools: A Python Library for Automated Preparation, Analysis, and Visualization of Kinetic Monte Carlo Simulations with Zacros. *J. Phys. Chem. A.* **2025**, *129* (29), 6608–6614.
(42) Wu, C.; Schmidt, D. J.; Wolverton, C.; et al. Accurate coverage-dependence incorporated into first-principles kinetic models: Catalytic NO oxidation on Pt (111). *J. Catal.* **2012**, *286*, 88–94.
(43) Prats, H.; Stamatakis, M. First-Principles Kinetic Monte Carlo Simulations for Single-Cluster Catalysis: Study of CO_2 and CH_4 Conversion on Pt/HfC. *ACS Catal.* **2025**, *15*, 2904–2915.
(44) Jones, G.; Jakobsen, J.; Shim, S. et al. First principles calculations and experimental insight into methane steam reforming over transition metal catalysts. *J. Catal.* **2008**, *259* (1), 147–160.
(45) Wei, J.; Iglesia, E. Isotopic and kinetic assessment of the mechanism of reactions of CH_4 with CO_2 or H_2O to form synthesis gas and carbon on nickel catalysts. *J. Catal.* **2004**, *224* (2), 370–383.

https://doi.org/10.1021/acscatal.6c01172
ACS Catal. XXXX, XXX, XXX–XXX

(46) Fan, C.; Zhu, Y.-A.; Yang, M.-L.; et al. Density Functional Theory-Assisted Microkinetic Analysis of Methane Dry Reforming on Ni Catalyst. *Ind. Eng. Chem. Res.* **2015**, *54* (22), 5901–5913.
(47) Yadavalli, S. S.; Jones, G.; Fonte, C.; et al. Elucidating the role of potassium in methane steam reforming using first-principles-based kinetic Monte Carlo simulations. *J. Catal.* **2025**, *448*, No. 116203.
(48) Pashchenko, D.; Makarov, I. Carbon deposition in steam methane reforming over a Ni-based catalyst: Experimental and thermodynamic analysis. *Energy* **2021**, *222*, No. 119993.
(49) Helveg, S.; Sehested, J.; Rostrup-Nielsen, J R Whisker carbon in perspective. *Catal. Today* **2011**, *178* (1), 42–46.

https://doi.org/10.1021/acscatal.6c01172
ACS Catal. XXXX, XXX, XXX–XXX